Violation of the Condon Approximation in Semiconducting Carbon Nanotubes

Juan G. Duque,[†,‡] Hang Chen,[§] Anna K. Swan,[§] Andrew P. Shreve,[†] Svetlana Kilina,[†] Sergei Tretiak,[†] Xiaomin Tu,[⊥] Ming Zheng,[⊥] and Stephen K. Doorn[†,*]

[†]Center for Integrated Nanotechnologies, MPA-CINT, MS-K771, [‡]Chemistry Division, Physical Chemistry and Applied Spectroscopy (C-PCS), Los Alamos National Laboratory, Los Alamos, New Mexico 87545, United States, [§]Department of Electrical and Computer Engineering, and Photonics Center, Boston University, Boston, Massachusetts 02215, United States, and [⊥]Polymers Division, National Institute of Standards and Technology, 100 Bureau Drive, Stop 8540, Gaithersburg, Maryland 20899-8540, United States

ABSTRACT The Condon approximation is widely applied in molecular and condensed matter spectroscopy and states that electronic transition dipoles are independent of nuclear positions. This approximation is related to the Franck–Condon principle, which in its simplest form holds that electronic transitions are instantaneous on the time scale of nuclear motion. The Condon approximation leads to a long-held assumption in Raman spectroscopy of carbon nanotubes: intensities arising from resonance with incident and scattered photons are equal. Direct testing of this assumption has not been possible due to the lack of homogeneous populations of specific carbon nanotube chiralities. Here, we present the first complete Raman excitation profiles (REPs) for the nanotube G band for 10 pure semiconducting chiralities. In contrast to expectations, a strong asymmetry is observed in the REPs for all chiralities, with the scattered resonance always appearing weaker than the incident resonance. The observed behavior results from violation of the Condon approximation and originates in changes in the electronic transition dipole due to nuclear motion (non-Condon effect), as confirmed by our quantum chemical calculations. The agreement of our calculations with the experimental REP asymmetries and observed trends in family dependence indicates the behavior is intrinsic.

KEYWORDS: carbon nanotube · Raman · G band · exciton–phonon coupling · spectroscopy

The low-dimensional carbon nanomaterials, graphene and single-walled carbon nanotubes (SWNTs), represent an intriguing nanoscale laboratory for studying fundamental quantum behaviors, quasi-particle interactions, and the limits of the approximations we use for understanding them. Remarkably, electrons in graphene and metallic SWNTs behave as Dirac Fermions.[1−5] SWNTs show strong exciton binding energies leading to complex energy levels and effective many-body phenomena such as impact ionization.[6,7] SWNTs also display a fascinating array of electron–phonon (e–ph) coupling behaviors including strong structural dependences,[8−12] phonon bottlenecks,[13] and related electron-vibrational dynamics such as coherent phonon generation.[14,15] In both graphene and metallic SWNTs, the e–ph interactions violate one of the core constructs used for understanding quantum mechanical behavior in many-body systems: the adiabatic Born–Oppenheimer approximation.[16−18] While the Born–Oppenheimer approximation holds in semiconducting nanotubes, we here demonstrate the failure of another fundamental principle underlying our understanding of e–ph interactions: the Franck–Condon approximation, which states that the electronic transition moment dipole is independent of nuclear coordinates and provides a picture of vertical electronic transitions occurring in the absence of nuclear motion along vibrational coordinates. Introduction of a nuclear coordinate dependence through non-Condon effects will have important consequences for a range of SWNT photophysical behaviors. Expected impacts on such processes as exciton generation; exciton diffusion, relaxation dynamics, and quantum yield;[19−23] and multiexciton interactions[6,7] are likely to affect related applications in photonics, optoelectronics, quantum optics, energy harvesting, and sensing.

While the consequences of nonadiabatic and non-Condon effects are familiar in molecular systems,[24,25] the existence of non-Condon activity is not typically considered when describing solid-state systems. However, the molecular concept of the Condon approximation is often extended to solid-state systems, particularly in describing electronic excitation of defects, dopants, and single molecules embedded in a solid matrix.[26,27] Electronic excitations in these localized species couple to the phonon modes of the solid, but the transition dipole is typically described as being independent of the phonon mode coordinates in a direct

* Address correspondence to skdoorn@lanl.gov.

Received for review April 18, 2011 and accepted May 26, 2011.

Published online May 26, 2011
10.1021/nn201430z

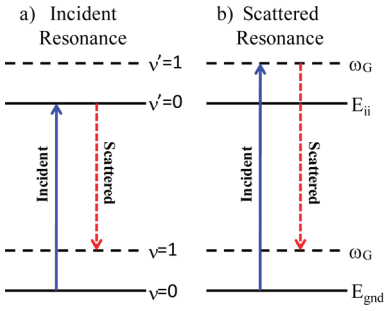

Figure 1. Depiction of SWNT resonance Raman scattering processes between ground (ν = 0,1) and excited-state (ν' = 0,1) phonon levels. Incident and scattered photon energies are shown by solid and dashed arrows, respectively. Two peaks separated by the G-phonon energy (ω_G) are expected in the SWNT REP arising from (a) incident resonance, incident photon energy = transition energy (E_{ii}); and (b) scattered resonance, scattered photon energy = E_{ii}.

analogy to the molecular description.[26,27] Strong parallels may be seen between such defect states and excitons in SWNTs when the excitons are viewed as localized excitations that couple to the phonon modes of the extended SWNT lattice. While the excitons may be viewed as molecular in nature, the solid-state picture of excitations coupling to phonons (rather than "molecular-like" localized vibrations) is retained. Thus, the importance of the non-Condon effect observed here illustrates that carbon nanotubes may also serve as an interesting bridge between the worlds of molecular chemistry and condensed matter physics.

Revelation of the significance of the non-Condon effects, important not just in Raman processes but for other photophysical behaviors as well, indicates that the fundamental basis of our understanding of Raman scattering in SWNTs must be re-evaluated. Raman spectroscopy of SWNTs has been instrumental for probing SWNT structure and for developing insight into the family and branch-dependent structure of SWNT electronic properties,[28−32] their electron−phonon coupling dependences,[8−12] and understanding other coupled electronic and vibrational behaviors such as electron transport.[33−35] Sensitivity of the Raman excitation profile (REP) to e−ph coupling also makes it an ideal tool for probing non-Condon effects. The Raman scattering process in SWNTs (depicted schematically in Figure 1) is expected to result in two peaks in the REP due to resonances with incident and scattered photons. A long-held assumption in the Raman spectroscopy of SWNTs has been that these two resonance peaks should be equal in intensity. This assumption is implicit in commonly used band-to-band and exciton models for Raman in SWNTs (see also Supporting Information).[8,29,31,32,36−40] Despite the importance of having accurate models for Raman scattering in SWNTs, this assumption has never been properly tested. While REPs of SWNT radial breathing modes (RBMs) for an extensive range of chiralities are readily obtained,[29,31,32,41] the low RBM frequency (~200 cm^{-1}) prevents resolution of the REP ingoing and outgoing resonances. The higher frequency (~1590 cm^{-1}) G band can allow resolution, but because its frequency is only weakly dependent on chirality, it is impossible to isolate the pure G-band response for a specific chirality in a mixed-chirality ensemble. Samples must therefore be highly enriched in a single chirality so that the pure G-band response of a single species may be accessed.

TABLE 1. Fitting Analysis of Raman Excitation Profiles[a]

			M_2/M_1		C	
(n,m)	E_{22} (eV)	Γ (eV)	G^+	G^-	G^+	G^-
(9,1)	1.755	0.038	−0.69		0.18	
(8,3)	1.846	0.033	−0.81		0.10	
(7,5)	1.903	0.034	−0.79	−0.71	0.12	0.17
(7,6)	1.899	0.037	−0.68	−0.59	0.19	0.26
(8,7)	1.685	0.038	−0.64		0.22	
(9,5)	1.829	0.043	−0.68		0.19	
(10,5)	1.554	0.028	−0.69	−0.53	0.18	0.31
(10,2)	1.674	0.026	−0.76	−0.65	0.14	0.21
(9,4)	1.711	0.029	−0.42	−0.37	0.41	0.46
(8,6)	1.719	0.031	−0.38	−0.32	0.45	0.51

[a] Best fit values for E_{22}, Γ, matrix element ratios (see eq 3), and resultant non-Condon parameter C (see eqs 8 and 9) obtained from applying the four-level model to experimental REP data for each nanotube chirality.

Here, we present G-band REP data obtained from samples highly enriched in single chiralities. In striking contrast to previous expectations, a strong asymmetry in the REP is discovered, with the incident resonance always being more intense than the scattered resonance response. Quantum chemical calculations confirm that there is a substantial change in the transition dipole as a function of the G-band coordinate; that is, a significant non-Condon contribution is predicted. The asymmetric REP response can therefore be understood as a violation of the Condon approximation, with asymmetries arising from quantum interference between Condon and non-Condon contributions. Surprisingly, we find the magnitude of the non-Condon contributions shows the reverse dependence on nanotube chirality in comparison to that found for exciton−phonon coupling in nanotubes. Agreement of that dependence with our quantum chemical calculations suggests the non-Condon effects are intrinsic.

RESULTS AND DISCUSSION

G-Band Spectroscopy of Pure-Chirality Samples. Raman spectra from bulk solutions of 10 SWNT samples (each highly enriched in the single chiralities listed in Table 1, identified by their chiral indices (n,m)) were acquired with excitation into the second nanotube exciton transition (E_{22}) across a range of wavelengths (see Methods). These samples were generated using ion-exchange chromatography of HiPco-produced samples of nanotubes suspended with selected DNA

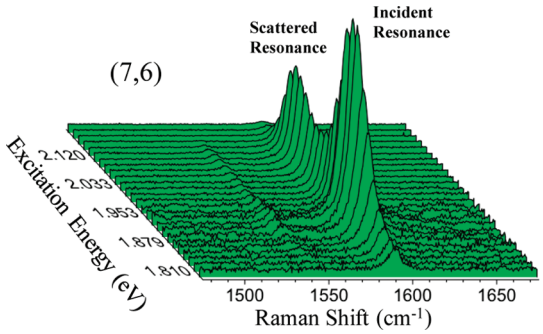

Figure 2. Plot of each G-band spectrum, showing both the G^+ and G^- peaks used in generating the REPs for the (7,6) chirality. Spectra are obtained with excitation wavelengths from 565 to 690 nm (2.198 to 1.797 eV). The locations of the resonances with incident and scattered photons are indicated. Each spectrum has been corrected for varying wavelength dependence of the instrument response.

sequences (for complete details, see ref 42). After isolation, samples were dialyzed into aqueous 1% deoxycholate. Absorbance and Raman spectra show the samples to have little or no contamination from other chiralities (Figures S1–S4, Supporting Information).

An example set of Raman spectra of the G-band region for the (7,6) chirality is shown in Figure 2 (see also Supporting Information Figure S5 for additional examples), with the G^+ feature appearing at 1591 cm^{-1} (± 1 cm^{-1}) and the weaker G^- peak appearing at 1543 cm^{-1}. Frequencies remain constant over all excitation wavelengths. A plot of the G^+ intensity (corrected for instrument response) as a function of excitation energy is shown in Figure 3 for each of our 10 chiralities. The two resonances appearing in the REPs are clearly resolved for each case. We observe the striking result that the scattered resonance for all chiralities is significantly weaker than the incident resonance. This asymmetric behavior in the resonance Raman response is found to be a general result across five different $2n + m$ families (=19, 20, 22, 23, and 25), for both mod 1 and mod 2 SWNTs (defined as mod$(n-m,3) = 1$ or 2, respectively), and over a wide range of diameters (between 0.757 and 1.05 nm). The degree of asymmetry varies with chirality. As seen in Figure 4, a similar result is found for the G^- peak: in all cases, the scattered resonance intensities are weaker than those for the incident resonance.

The REP asymmetry reveals that the assumption of equal intensities built into the commonly used band-to-band and exciton models is inadequate for describing the SWNT Raman response (see also Supporting Information Figure S7). Instead, excellent fits to the experimental data (Figures 3 and 4) may be obtained by using a four-level model commonly used for describing Raman scattering in molecular systems.[25] Such a model begins with a standard Kramers–Heisenberg description of Raman scattering, with the Raman intensity (I_{RRS}), after orientational averaging over an isotropic sample, being proportional to the sum of squares of the polarizability components ($\alpha_{\rho\sigma}$) (eq 1) and $\alpha_{\rho\sigma}$ is defined in eq 2.[43]

$$I_{RRS} \propto \sum_{\rho\sigma} |\alpha_{\rho\sigma}|^2 \quad (1)$$

$$\alpha_{\rho\sigma} = \sum_{\nu} \left[\frac{\langle f|\mu_\rho|\nu\rangle\langle\nu|\mu_\sigma|g\rangle}{E_\nu - E_g - E_L - i\Gamma} + \mathrm{NR} \right] \quad (2)$$

Here, ρ and σ represent the Cartesian components of the transition moment dipole operator (μ). Scattering involves the initial $|g\rangle$, final $|f\rangle$, and set of intermediate $|\nu\rangle$ states of energies E_g, E_f, and E_ν, respectively. E_L is the energy of incident photons, Γ is a damping factor, and NR designates nonresonant contributions. In the limit of weak electron–phonon coupling (appropriate for SWNTs; see Supporting Information and ref 12), only the four states shown in Figure 1 contribute significant amplitude to $\alpha_{\rho\sigma}$. The sum over excited states (ν) in eq 2 then only includes the first two terms $\nu = 0$ and 1. With the optical transitions polarized along the SWNT axis, one can choose a coordinate system in which only one of the Cartesian components of α is nonzero. In this limit, eq 2 reduces to our four-level model of eq 3:

$$I_{RRS} \propto \left| \frac{M_1}{i(E_L - E_{ii}) + \Gamma} + \frac{M_2}{i(E_L - E_{ii} - E_{ph}) + \Gamma} \right|^2 \quad (3)$$

From eq 3, I_{RRS} varies as laser excitation energy (E_L) is tuned across a specific transition (E_{ii}) and depends on the phonon frequency of interest (E_{ph}). In eq 3, M_1 and M_2 represent matrix elements for resonance with incident and scattered photons, respectively, as defined in Figure 1. Within this model, an asymmetric response occurs when M_1 and M_2 are not equal. The discrete nature of the SWNT excitonic transitions and strongly correlated electron–hole interactions, paired with momentum conservation requirements that limit optical activity to the zone center, resemble a discrete electronic two-level system, more reminiscent of a molecule than an extended solid-state system, thus justifying use of such a model.

Fitting to this model is performed by fixing the G-band frequency to the experimentally measured value, while values for M_1, M_2, Γ, and E_{22} in eq 3 are adjustable parameters, with the best fit results for each chirality given in Table 1. The phonon frequency used in eq 3 is more accurately the excited-state value. Adjusting this value in the fits, however, results in large variability from the measured ground-state frequency that could be as high as 100 cm^{-1}, without significant improvement in the fits. Therefore, in the absence of accurate excited-state frequencies, the ground-state values are retained. The quality of the fits is further highlighted in that the generated E_{22} values match those obtained from simultaneously measured RBM excitation profiles and are also in excellent agreement

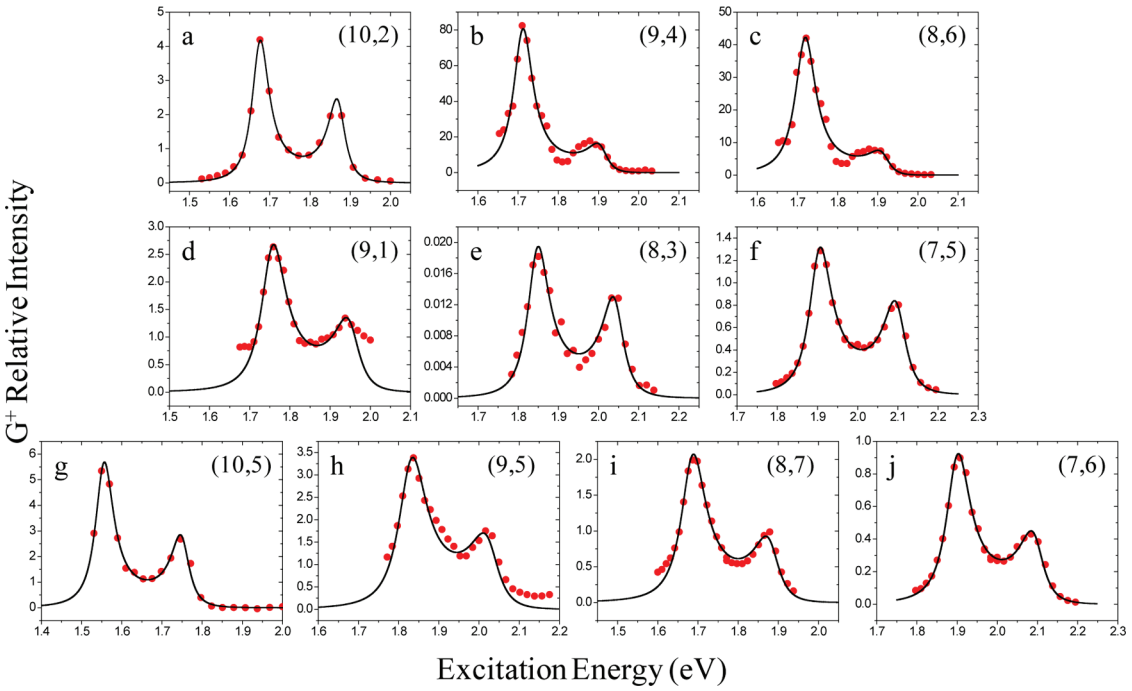

Figure 3. Resonance Raman excitation profiles for the G^+ peak. Relative intensity of the G^+ peak (1591 cm^{-1}) as excitation energy is varied for 10 SWNT chiralities identified by their chiral indices (*n*,*m*): (a) (10,2); (b) (9,4); (c) (8,6); (d) (9,1); (e) (8,3); (f) (7,5); (g) (10,5); (h) (9,5); (i) (8,7); (j) (7,6). Circles are experimental data with solid line being best fit of eq 3 to the data. Fitting parameters are given in Table 1. (Signal-to-noise ratio of individual G^+ intensities with excitation at the resonance maxima are typically >100.)

with those obtained from the absorption spectra (Supporting Information Table S1). It is important to note that the experimental data are fit well using identical Γ values for incoming and outgoing resonances for a specific chirality, indicating that the asymmetry in the profiles does not arise from line-broadening effects and their impact on observed intensities, but originates instead in differences in the magnitude of the matrix elements for the two scattering processes. For G^+, we find ratio values of M_2/M_1 range from -0.38 to -0.81 and are negative in all cases. A similar range in values (from -0.32 to -0.71; see Table 1) is found for the G^- peak.

Non-Condon Effects. The asymmetry observed in Figures 3 and 4 runs counter to long-held expectations for Raman response in SWNTs and cannot be explained within traditional frameworks for understanding Raman scattering in condensed matter systems. Given the successful four-level modeling of the response, coupled with the many "molecular" characteristics of the SWNT excitonic transitions, it should not be surprising that parallel behaviors might be found in the Raman profiles of certain molecular systems. In fact, excitation profiles of select high frequency modes ($\sim$1600 cm^{-1}) in metalloporphyrins display similarly strong asymmetries with excitation into their Q band.[25] This behavior is understood as a consequence of a breakdown in the Franck–Condon approximation, generalized as a vibrational coordinate dependence in the electronic transition-moment dipole operator (μ) of eq 2 for excitation and emission processes. Given the similarity in response between SWNTs and metalloporphyrins, it is likely that such non-Condon effects are also responsible for the observed behavior in SWNTs. Additionally, a previous analysis of excitation profiles for RBM fundamental and overtone vibrations indirectly suggested the presence of non-Condon effects in SWNTs.[12]

Non-Condon effects are modeled in molecular systems by expanding μ in a Taylor series about the equilibrium geometry of the nuclear coordinates (q_0) for the normal mode of interest:[25]

$$\mu = \mu_0 + \left(\frac{\partial \mu}{\partial q}\right)_o q + \cdots \quad (4)$$

with higher order terms neglected. By substituting the right-hand side of eq 4 into eq 2, the first-order expansion is then seen to give rise to the commonly defined Albrecht *A*-term (Condon) and *B*-term (non-Condon) contributions to the Raman polarizability[25,43] (see also Supporting Information), as given in eqs 5 and 6:

$$A_{\rho\sigma} = \mu^o_\rho \mu^o_\sigma \sum_\nu \frac{\langle f|\nu\rangle\langle\nu|g\rangle}{E_\nu - E_g - E_L - i\Gamma} \quad (5)$$

$$B_{\rho\sigma} = \mu^o_\rho \mu'_\sigma \sum_\nu \frac{\langle f|\nu\rangle\langle\nu|q|g\rangle}{E_\nu - E_g - E_L - i\Gamma} + \mu'_\sigma \mu^o_\rho \sum_\nu \frac{\langle f|q|\nu\rangle\langle\nu|g\rangle}{E_\nu - E_g - E_L - i\Gamma} \quad (6)$$

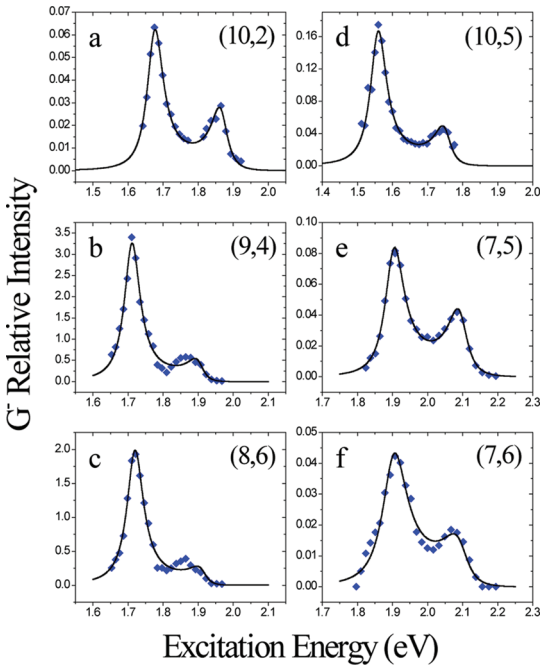

Figure 4. Resonance Raman excitation profiles for the G^- peak. Relative intensity of the G^- peak as excitation energy is varied for six SWNT chiralities identified by their chiral indices (*n*,*m*): (a) (10,2); (b) (9,4); (c) (8,6); (d) (10,5); (e) (7,5); (f) (7,6). Diamonds are experimental data with solid line being best fit of eq 3 to the data. Fitting parameters are given in Table 1.

In eqs 5 and 6, $\mu' = (d\mu/dq)_0$. The Raman polarizability then becomes the sum of the Condon and non-Condon contributions:

$$\alpha_{\rho\sigma} = A_{\rho\sigma} + B_{\rho\sigma} \quad (7)$$

In the limit of weak exciton−phonon coupling, the Condon contributions to the Raman response are expected to be equal in intensity for the two resonance conditions but opposite in sign (see ref 25 and Supporting Information eqs S11 and S12), accounting for the opposite sign found for M_1 and M_2 in the four-level fitting results. Ultimately, the weak exciton−phonon coupling is also the reason behind our ability to observe the non-Condon effect. In many strongly coupled systems, the Condon-active terms will dominate the scattering response. In weakly coupled systems, however, the magnitude of the Condon and non-Condon terms becomes more on par, allowing non-Condon effects to be observed in the REPs. Differences in the relative phasing and magnitude of the Condon and non-Condon contributions are responsible for the decrease in intensity of the second resonance. The non-Condon contribution thus introduces a self-interference effect that produces the final REP asymmetry[25,44] (Supporting Information Figure S8). While interference between closely spaced electronic states has been recognized as a route to Raman interference in SWNTs,[8,45,46] interference arising from non-Condon effects represents a new mechanism that has not previously been considered in carbon nanotubes.

The REP data can be used to quantify the degree of non-Condon contributions to the Raman polarizability as follows. We begin by defining a non-Condon parameter *C* that is a relative measure of the *B*-term contribution (see Supporting Information):

$$C = [(\partial\mu/\partial q)_0/\mu_0] \times 1/\sqrt{2S} \quad (8)$$

where the Huang−Rhys factor $S = \Delta^2/2$, with Δ being the excited-state displacement along the phonon normal mode coordinate. Furthermore, in the limit of weak exciton−phonon coupling (small *S*), the ratio of the matrix elements of eq 3 can be shown to be directly related to *C* (see Supporting Information):

$$\frac{M_2}{M_1} = \frac{-(1-C)}{(1+C)} \quad (9)$$

The *C* values derived from our fits to the REPs are given in Table 1 and range from 0.10 to 0.45 for G^+ and 0.17 to 0.51 for G^-. The magnitude of the *C* values indicates that non-Condon effects are important in carbon nanotubes and the G-mode phonon is capable of significant perturbation of the electronic transition moment. In comparing the G^- and G^+ C values for the six chiralities for which we could obtain both, we note that *C* is ~50% larger in the G^- case for all chiralities. The difference in non-Condon activity of each mode likely arises from the difference in how each couples to the exciton transition. Understanding the origins of this difference in behavior is the subject of continuing investigation.

Quantum Chemical Calculations. The demonstrated significance of the non-Condon effects makes it important to explore their origins. Our strategy is to use quantum chemical calculations[12,47,48] to determine the degree to which displacement along the G-mode coordinate affects the electronic transition moment dipole, thus allowing a theoretical determination of expected *C* values. Our focus is on the G^+ phonon. We begin by calculating E_{11} and E_{22} absorption spectra for the (7,6) and (9,4) geometries, as disturbed by varying the G^+ coordinate displacement (Δ) (Supporting Information Figure S9). A plot of the difference in squares of the transition dipole (determined from the calculated absorption spectra) between the disturbed and undisturbed geometries as a function of displacement along the G^+ coordinate is shown in Figure 5. Comparison with eq 4 shows that the slope of each line in Figure 5 is twice the quantity $(\partial\mu/\partial q)_0/\mu_0$, which is used along with calculated values (see Supporting Information) of the excited-state displacement (Δ = −0.35 for (7,6) and +0.45 for (9,4) for E_{22} transitions) to generate a calculated non-Condon parameter *C*, as per eq 8.

For the E_{22} transitions, the calculated values of C are 0.067 for the (7,6) case and 0.17 for the (9,4) case. Corresponding experimental values are 0.19 for the (7,6) case and 0.41 for the (9,4) case. The calculated values are systematically smaller than the experimental values in each case, possibly arising from an overestimation of Δ (see Supporting Information). However, the ratios of C for the (9,4) to (7,6) cases are in good agreement, 2.5 (calculated) and 2.2 (experimental), giving confidence that the non-Condon effects as manifested in the REPs originate in a coordinate dependence in the electronic transition moment dipole. It is also interesting to note that the slopes obtained for E_{11} differ by a factor of 2 from those found for E_{22}, but are in opposite directions for the two species. On going to E_{11} from E_{22}, the magnitude of the (7,6) slope increases (0.082 *vs* −0.047), while the (9,4) slope decreases (−0.070 *vs* 0.149), suggesting a significant E_{ii} dependence in the non-Condon effects.

Chirality Dependence of Non-Condon Effects. As with other SWNT optical properties and suggested by the quantum chemical results, it is reasonable to expect a significant chirality, mod, and E_{ii} dependence in the observed non-Condon behavior. The relation between these parameters and the observed REP asymmetry is not directly obvious in the REPs themselves, but by plotting the C values for G^+ as a function of diameter (d) (see Figure 6a), some trends become apparent. First, C is seen to be a weak function of nanotube diameter, increasing as d increases. Also, within the $2n + m = 22$ family, there is a clear dependence of C on chiral angle (θ), with C increasing as θ increases from the (10,2) through (8,6) structures. Although not as pronounced, a similar trend is also seen for the $2n + m = 23$ and 19 families. These same trends are also found in the G^- behavior (see Table 1). (We note the (9,1) chirality appears to lie outside of this trend. However, its C value may have significant uncertainty due to the presence of impurity chiralities, as reflected in its larger error bars (see also Supporting Information Figures S3 and S4.) In determining the structural dependence of the non-Condon effects, ideally one would want to explore trends purely in $[(\partial\mu/\partial q)_0/\mu_0]$. In eq 8, however, it is seen that the C factor also includes a contribution from the exciton−phonon coupling through S, which is also chirality-dependent.[8−12] It has been shown theoretically, however, that the chirality dependence of S for the G band is relatively weak,[49] and we find factoring it out of eq 8 by using theoretical S values[49] does not significantly alter the trends observed in Figure 6a.

The trends in diameter and chiral angle both appear anticorrelated to expectations for the strength of the exciton−phonon coupling in nanotubes (related to S).[8−10] This is further suggested in that the C values for G^- (with significantly weaker coupling than G^+) are found to be larger than for G^+. Whether the structural dependence of C and S are connected remains an open question. Alternatively, the diameter dependence of C may originate in it being a relative measure of how the electronic transition moment changes with nuclear coordinate in relation to the unperturbed value (μ_0). As with S, μ_0 is also expected to decrease as diameter increases.[49] The complex chiral angle, mod, and E_{ii} dependence may then be introduced through effects on $\partial\mu/\partial q$. To some degree, this may result from the curvature of the potential energy surfaces experienced for specific exciton transitions. The positions of the band minima within the graphene Brillouin zone for the E_{22} transition of each chirality are represented in Figure 6b. Equal energy contour lines shown in this plot are distorted due to the effects of trigonal warping[50,51] and display a greater degree of curvature at higher energies along the K−M direction. The minima for the mod 1 structures are found to cluster in a region of similar curvature, possibly explaining their similar C values. The greater spread in C found for mod 2 structures likely results from their sampling a larger region of the Brillouin zone. The quantum chemical calculations are also suggestive of the importance of the band curvature. With E_{11} excitation, we find that there is less of a difference between the mod 1 and mod 2 values for $\partial\mu/\partial q$ (Figure 5). This is also an expected result for band curvature. As one moves closer to the K point within the Brillouin zone on going from E_{22} to E_{11} excitation, the effects of trigonal warping on band structure are much less pronounced, giving the

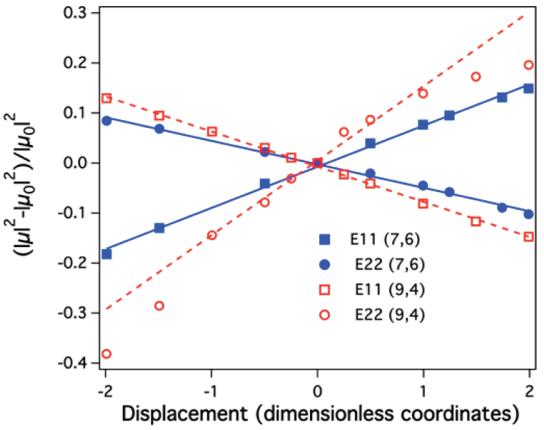

Figure 5. Vibrational coordinate dependence of the transition moment dipole. Plots of the change of the square of transition dipole (μ) *versus* coordinate displacement (Δ) along the G^+ mode, normalized by the square of the transition dipole with no distortion (μ_0). The values of the square of transition dipoles are calculated as the sum of this quantity over all transitions contributing to the first (E_{11}, squares) or second (E_{22}, circles) excitonic features (see Supporting Information), with solid blue symbols for the (7,6) case and open red symbols for the (9,4) case. For all sets of data except the E_{22} (9,4) case, the lines (dashed for (9,4) and solid for (7,6)) are linear fits to the entire data set. For the E_{22} (9,4) case, the line is derived from a linear fit only to values of displacement between −1 and +1 (note that a second-order polynomial fit to the E_{22} (9,4) data yields excellent agreement over the entire range and has a linear term matching that from the linear fit over −1 to +1).

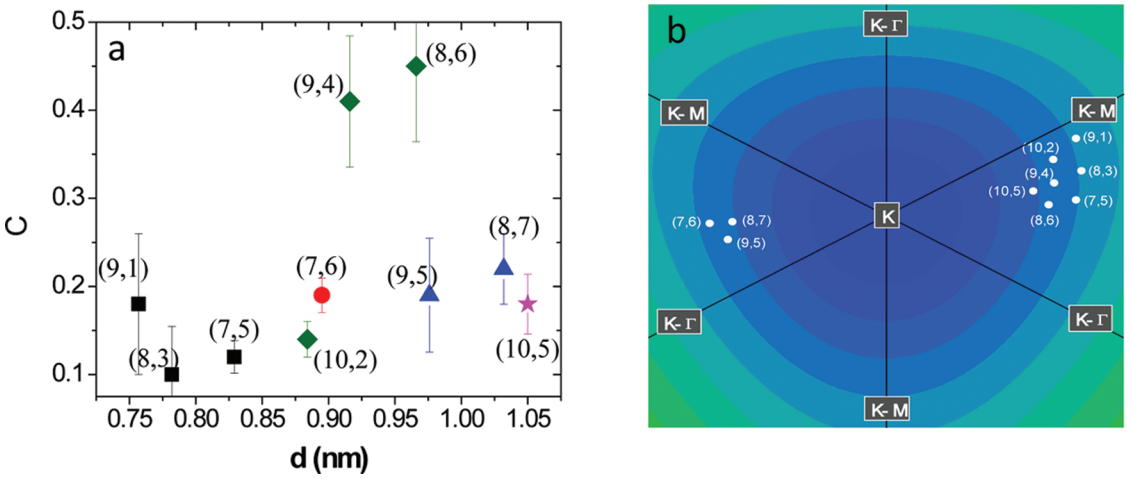

Figure 6. Chirality dependence of the non-Condon effect. (a) Plot of the magnitude of the non-Condon parameter *C* for G^+ as a function of SWNT diameter for the 10 chiralities of Figure 3 [(*n*,*m*) indices labeled]. Identical symbols are used for species of the same $2n + m$ family: $2n + m = 25$, stars; 23, triangles; 22, diamonds; 20, circles; 19 squares. (b) Graphene Brillouin zone showing equal-energy contour lines centered on the *K* point and with the high-symmetry *K*−*M* and *K*−Γ lines labeled. Positions of band minima for each chirality are shown as white circles.

expectation that behavior will be more similar for mod 1 and mod 2 structures.

The structural dependence of the non-Condon behavior in SWNTs is thus likely to be a complex function of several interconnected parameters. Gaining a quantitative understanding of these structural dependences is needed to clarify the origins of the breakdown in the Condon approximation in SWNTs and will require further experimental and theoretical effort. A useful starting point may be in exploring the potential of mixing of electronic states (for example, through a phonon-mediated Hertzberg−Teller (HT) coupling mechanism) to act as the physical origin of the intrinsic dependence of the electronic transition moment on vibrational coordinates. Such coupling can serve to shift oscillator strength out of the parent E_{22} state, effectively acting as a coordinate dependent change in the transition moment dipole. State mixing has previously been proposed as the origin of a rare example of REP asymmetry in solid-state systems. In GaAs/Al_xGa_{1-x}As quantum wells, asymmetry is suggested to arise from GaAs exciton states interacting or mixing with dopant-induced states of the $Al_xGa_{1-x}As$ interlayers.[52] It may be possible that the asymmetry we observe here also results from nanotube excitonic states mixing with dopant-induced states. However, our quantum chemical results suggest otherwise, showing that the asymmetry can arise directly from intrinsic nanotube behavior without the need to invoke doping. Instead, mixing is possible with a range of intrinsic bright, dark, or continuum states, with the number of states accessible for mixing increasing dramatically as one goes to higher excitation energies. Direct mixing of bright exciton states will be of particular interest for the E_{33} and E_{44} transitions, for which the energies in mod 2 structures approach and even cross each other as a result of trigonal warping.[53]

CONCLUSION

In summary, G-band REPs of pure-chirality semiconducting SWNT samples display a strong asymmetry in intensities for resonance with incident and scattered photons, contrary to long-held expectations for equal intensity in the two resonance peaks. The result calls for a re-evaluation of how we describe the Raman scattering process in SWNTs. We demonstrate and quantify the origins of this behavior as resulting from non-Condon effects, described as a vibrational coordinate dependence in the transition moment dipole. Beyond the observed effects on Raman response, the importance of the non-Condon effects should be considered for other aspects of nanotube photophysics, as well. Potential consequences include re-evaluating how we determine exciton−photon and exciton−phonon coupling from Raman data (ultimately dependent on details of the models used for analyzing Raman response) and how non-Condon effects impact the resultant matrix elements.[8,49,54] Of significant interest will be the potential that non-Condon effects have for generating phonon-mediated mixing of excited states. Such state mixing will impact a variety of excited-state processes, including dynamics and pathways for exciton relaxation, potential for carrier multiplication, and ultimately how observed quantum yield may vary with excitation regime. Viewed as molecules, the excitonic states of carbon nanotubes provide a useful laboratory for exploring a wide range of non-Condon behaviors due to their relatively simple and uncoupled phonon structure. This leads to an extremely clean spectral response not typically found in molecular systems comprising large numbers of often strongly coupled modes. As a result, assessing non-Condon behaviors in nanotubes may be a more tractable problem than in more

traditional molecular systems. In general, such a molecular point of view may be a useful perspective from which to understand other SWNT behaviors, as well. Further exploring and understanding the origins and consequences of non-Condon effects will thus be a fruitful new area for SWNT studies. Finally, these results further suggest the important role that the expanding availability of pure chirality samples will continue to play in revealing a wide range of new SWNT photophysics.

METHODS

Raman Spectroscopy. Raman spectra were obtained on bulk solution samples with excitation wavelengths ranging from 850 to 565 nm using a combination of tunable Ti:sapphire and dye lasers (kiton red and rhodamine 6G dyes), with typically 25 mW of incident power. Spectra are collected in a backscattering geometry through a triple monochromator and detected with a CCD using 2–5 min integration times. Intensities of all spectra were corrected for instrument response using benzonitrile (mode at 1598.9 cm^{-1}) as an intensity reference (demonstrated in Supporting Information Figure S6).

Quantum Chemical Calculations. See Supporting Information for details.

Acknowledgment. J.G.D., S.T., and S.K.D. acknowledge support from the LANL-LDRD program. A.K.S. acknowledges the support of NSF Grant DMR-0706574. S.K. acknowledges support from ND EPSCoR and NSF grant #EPS-0814442. X.T. and M.Z. acknowledge the support of NSF Grant CMS-060950. This work was performed in part at the Center for Integrated Nanotechnologies, a U.S. Department of Energy, Office of Basic Energy Sciences user facility.

Supporting Information Available: Discussion of sample purity. Examples of raw G-band spectra and illustration of the correction of G-band intensities for instrument response. A comparison of band-to-band, exciton, and four-level molecular models for REP behavior. The derivation of non-Condon contributions to the REPs leading to eqs 3, 8, and 9, with a discussion of non-Condon interference effects. Details on the quantum chemical calculations including the calculated absorption spectra as a function of coordinate displacement used in developing Figure 5. This material is available free of charge *via* the Internet at http://pubs.acs.org.

REFERENCES AND NOTES

1. Novoselov, K. S.; Geim, A. K.; Morozov, S. V.; Jiang, D.; Katsnelson, M. I.; Grigorieva, I. V.; Dubonos, S. V.; Firsov, A. A. Two Dimensional Gas of Massless Dirac Fermions in Graphene. *Nature* **2005**, *438*, 197–200.
2. Zhou, S. Y.; Gweon, G. H.; Graf, J.; Fedorov, A. V.; Spataru, C. D.; Diehl, R. D.; Kopelevich, Y.; Lee, D. H.; Louie, S. G.; Lanzara, A. First Direct Observation of Dirac Fermions in Graphite. *Nat. Phys.* **2006**, *2*, 595–599.
3. Geim, A. K.; Novoselov, K. S. The Rise of Graphene. *Nat. Mater.* **2007**, *6*, 183–191.
4. Castro Neto, A. H.; Guinea, F.; Peres, N. M. R.; Novoselov, K. S.; Geim, A. K. The Electronic Properties of Graphene. *Rev. Mod. Phys.* **2009**, *81*, 109–162.
5. Saito, R.; Fujita, M.; Dresselhaus, G.; Dresselhaus, M. S. Electronic Structure of Chiral Graphene Tubules. *Appl. Phys. Lett.* **1992**, *60*, 2204–2206.
6. Gabor, N. M.; Zhong, Z.; Bosnick, K.; Park, J.; McEuen, P. L. Extremely Efficient Multiple Electron–Hole Pair Generation in Carbon Nanotube Photodiodes. *Science* **2009**, *325*, 1367–1371.
7. Wang, S.; Khafizov, M.; Tu, X.; Zheng, M.; Krauss, T. D. Multiple Exciton Generation in Single-Walled Carbon Nanotubes. *Nano Lett.* **2010**, *10*, 2381–2386.
8. Jiang, J.; Saito, R.; Gruneis, A.; Chou, S. G.; Samsonidze, Ge. G.; Jorio, A.; Dresselhaus, G.; Dresselhaus, M. S. Intensity of the Resonance Raman Excitation Spectra of Single-Walled Carbon Nanotubes. *Phys. Rev. B* **2005**, *71*, 205420.
9. Machon, M.; Reich, S.; Telg, H.; Maultzsch, J.; Ordejon, P.; Thomsen, C. Strength of Radial Breathing Mode in Single-Walled Carbon Nanotubes. *Phys. Rev. B* **2005**, *71*, 035416.
10. Goupalov, S. V.; Satishkumar, B. C.; Doorn, S. K. Chirality and Excitation Dependence of Exciton–Phonon Coupling in Carbon Nanotubes. *Phys. Rev. B* **2006**, *73*, 115401.
11. Yin, Y.; Vamivakas, A. N.; Walsh, A. G.; Cronin, S. B.; Unlu, M. S.; Goldberg, B. B.; Swan, A. K. Optical Determination of Electron–Phonon Coupling in Carbon Nanotubes. *Phys. Rev. Lett.* **2007**, *98*, 037404.
12. Shreve, A. P.; Haroz, E. H.; Bachilo, S. M.; Weisman, R. B.; Tretiak, S.; Kilina, S.; Doorn, S. K. Determination of Exciton–Phonon Coupling Elements in Single-Walled Carbon Nanotubes *via* Raman Overtone Analysis. *Phys. Rev. Lett.* **2007**, *98*, 037405.
13. Steiner, M.; Freitag, M.; Perebeinos, V.; Tsang, J. C.; Small, J. P.; Kinoshita, M.; Yuan, D. N.; Liu, J.; Avouris, P. Phonon Populations and Electrical Power Dissipation in Carbon Nanotube Transistors. *Nat. Nanotechnol.* **2009**, *4*, 320–324.
14. Lim, Y. S.; Yee, K. J.; Kim, J. H.; Haroz, E. H.; Shaver, J.; Kono, J.; Doorn, S. K.; Hauge, R. H.; Smalley, R. E. Coherent Lattice Vibrations in Single-Walled Carbon Nanotubes. *Nano Lett.* **2006**, *6*, 2696–2700.
15. Luer, L.; Gadermaier, C.; Crochet, J.; Hertel, T.; Brida, D.; Lanzani, G. Coherent Phonon Dynamics in Semiconducting Carbon Nanotubes: A Quantitative Study of Electron–Phonon Coupling. *Phys. Rev. Lett.* **2009**, *102*, 127401.
16. Pisana, S.; Lazzeri, M.; Casiraghi, C.; Novoselov, K. S.; Geim, A. K.; Ferrari, A. C.; Mauri, F. Breakdown of the Adiabatic Born–Oppenheimer Approximation in Graphene. *Nat. Mater.* **2007**, *6*, 198–201.
17. Piscanec, S.; Lazzeri, M.; Robertson, J.; Ferrari, A. C.; Mauri, F. Optical Phonons in Carbon Nanotubes: Kohn Anomalies, Peierls Distortions, and Dynamic Effects. *Phys. Rev. B* **2007**, *75*, 035427.
18. Bushmaker, A. W.; Deshpande, V. V.; Hsieh, S.; Bockrath, M. W.; Cronin, S. B. Direct Observation of Born–Oppenheimer Approximation Breakdown in Carbon Nanotubes. *Nano Lett.* **2009**, *9*, 607–611.
19. Spataru, C. D.; Ismail-Beigi, S.; Capaz, R. B.; Louie, S. G. Theory and *Ab Initio* Calculation of Radiative Lifetimes in Semiconducting Carbon Nanotubes. *Phys. Rev. Lett.* **2005**, *95*, 247402.
20. Cognet, L.; Tsyboulski, D. A.; Rocha, J. D. R.; Doyle, C. D.; Tour, J. M.; Weisman, R. B. Step-Wise Quenching of Exciton Fluorescence in Carbon Nanotubes by Single-Molecule Reactions. *Science* **2007**, *316*, 1465–1468.
21. Carlson, L. J.; Maccagnano, S. E.; Zheng, M.; Silcox, J.; Krauss, T. D. Fluorescence Efficiency of Individual Carbon Nanotubes. *Nano Lett.* **2007**, *7*, 3698–3703.
22. Rajan, A.; Strano, M. S.; Heller, D. A.; Hertel, T.; Schulten, K. Length-Dependent Optical Effects in Single-Walled Carbon Nanotubes. *J. Phys. Chem. B* **2008**, *112*, 6211–6213.
23. Wang, F.; Dukovic, G.; Brus, L. E.; Heinz, T. F. Time-Resolved Fluorescence of Carbon Nanotubes and Its Implications for Radiative Lifetimes. *Phys. Rev. Lett.* **2004**, *92*, 177401.
24. Bunker, P. R.; Moss, R. E. Breakdown of Born–Oppenheimer Approximation: Effective Vibration–Rotation Hamiltonian for a Diatomic Molecule. *Mol. Phys.* **1977**, *33*, 417–424.
25. Kumble, R.; Rush, T. S.; Blackwood, M. E.; Kozlowski, P. M.; Spiro, T. G. Simulation of Non-Condon Enhancement and Interference Effects in the Resonance Raman Intensities of Metalloporphyrins. *J. Phys. Chem. B* **1998**, *102*, 7280–7286.

26. Huang, K.; Rhys, A. Theory of Light Absorption and Non-radiative Transitions in F-Centres. *Proc. R. Soc. A* **1950**, *204*, 406–423.
27. Dexter, D. L. Theory of Optical Properties of Imperfections in Nonmetals. In *Solid State Physics: Advances in Research and Applications*; Seitz, F., Turnbull, D., Eds.; Academic Press: San Diego, CA, 1958; Vol. 6, pp 353–411.
28. Rao, A. M.; *et al.* Diameter Selective Raman Scattering from Vibrational Modes in Carbon Nanotubes. *Science* **1997**, *275*, 187–191.
29. Telg, H.; Maultzsch, J.; Reich, S.; Hennrich, F.; Thomsen, C. Chirality Distribution and Transition Energies of Carbon Nanotubes. *Phys. Rev. Lett.* **2004**, *93*, 177401.
30. Araujo, P. T.; Doorn, S. K.; Kilina, S.; Tretiak, S.; Einarsson, E.; Maruyama, S.; Chacham, H.; Pimenta, M. A.; Jorio, A. Third and Fourth Optical Transitions in Semiconducting Carbon Nanotubes. *Phys. Rev. Lett.* **2007**, *98*, 067401.
31. Strano, M. S.; Doorn, S. K.; Haroz, E.; Kittrell, C.; Hauge, R. H.; Smalley, R. E. Assignment of (*n*,*m*) Raman and Optical Features of Metallic Single-Walled Carbon Nanotubes. *Nano Lett.* **2003**, *3*, 1091–1096.
32. Fantini, C.; Jorio, A.; Souza, M.; Strano, M. S.; Dresselhaus, M. S.; Pimenta, M. A. Optical Transition Energies for Carbon Nanotubes from Resonant Raman Spectroscopy: Environment and Temperature Effects. *Phys. Rev. Lett.* **2004**, *93*, 147406.
33. Yao, Z.; Kane, C. L.; Dekker, C. High-Field Electrical Transport in Single-Walled Carbon Nanotubes. *Phys. Rev. Lett.* **2000**, *84*, 2941–2944.
34. Suzuura, H.; Ando, T. Phonons and Electron–Phonon Scattering in Carbon Nanotubes. *Phys. Rev. B* **2002**, *65*, 235412.
35. Perebeinos, V.; Tersoff, J.; Avouris, P. Electron–Phonon Interaction and Transport in Semiconducting Carbon Nanotubes. *Phys. Rev. Lett.* **2005**, *94*, 086802.
36. Martin, R. M.; Falicov, L. M. Resonant Raman Scattering. In *Light Scattering in Solids I, Topics in Applied Physics*, 2nd ed.; Cardona, M., Ed.; Springer-Verlag: Berlin, 1983; Vol. 8, pp 79–146.
37. Canonico, M.; Adams, G. B.; Poweleit, C.; Menendez, J.; Page, J. B.; Harris, G.; van der Meulen, H. P.; Calleja, J. M.; Rubio, J. Characterization of Carbon Nanotubes Using Raman Excitation Profiles. *Phys. Rev. B* **2002**, *65*, 201402(R).
38. Thomsen, C.; Reich, S. Raman Scattering in Carbon Nanotubes. In *Light Scattering in Solids IX, Topics in Applied Physics*; Springer-Verlag, Berlin, 2007; Vol. 108, pp 115–232.
39. Pimenta, M. A.; Marucci, A.; Empedocles, S. A.; Bawendi, M. G.; Hanlon, E. B.; Rao, A. M.; Eklund, P. C.; Smalley, R. E.; Dresselhaus, G.; Dresselhaus, M. S. Raman Modes of Metallic Carbon Nanotubes. *Phys. Rev. B* **1998**, *58*, 16016(R).
40. Vamivakas, A. N.; Walsh, A.; Yin, Y.; Unlu, M. S.; Goldberg, B. B.; Swan, A. K. Exciton-Mediated One-Phonon Resonant Raman Scattering from One-Dimensional Systems. *Phys. Rev. B* **2006**, *74*, 205405.
41. Doorn, S. K.; Heller, D. A.; Barone, P. W.; Usrey, M. L.; Strano, M. S. Resonant Raman Excitation Profiles of Individually Dispersed Single-Walled Carbon Nanotubes in Solution. *Appl. Phys. A: Mater. Sci. Process.* **2004**, *78*, 1147–1155.
42. Tu, X.; Manohar, S.; Jagota, A.; Zheng, M. DNA Sequence Motifs for Structure-Specific Recognition and Separation of Carbon Nanotubes. *Nature* **2009**, *460*, 250–253.
43. Albrecht, A. C. On the Theory of Raman Intensities. *J. Chem. Phys.* **1961**, *34*, 1476–1484.
44. Clark, R. J. H.; Dines, T. J. Interference between *A*- and *B*-Term Resonance Raman Scattering for Totally Symmetric Modes. *Chem. Phys. Lett.* **1981**, *79*, 321.
45. Bussi, G.; Menendez, J.; Ren, J.; Canonico, M.; Molinari, E. Quantum Interferences in the Raman Cross Section for the Radial Breathing Mode in Metallic Carbon Nanotubes. *Phys. Rev. B* **2005**, *71*, R041404.
46. Son, H.; Reina, A.; Samsonidze, G. G.; Saito, R.; Jorio, A.; Dresselhaus, M. S.; Kong, J. Raman Characterization of Electronic Transition Energies of Metallic Single-Wall Carbon Nanotubes. *Phys. Rev. B* **2006**, *74*, 073406.
47. Tretiak, S.; Saxena, A.; Martin, R. L.; Bishop, A. R. Conformational Dynamics of Photoexcited Conjugated Molecules. *Phys. Rev. Lett.* **2002**, *89*, 097402.
48. Kilina, S.; Tretiak, S. Excitonic and Vibrational Properties of Single-Walled Semiconducting Carbon Nanotubes. *Adv. Funct. Mater.* **2007**, *17*, 3405–3420.
49. Jiang, J.; Saito, R.; Sato, K.; Park, J. S.; Samsonidze, Ge. G.; Jorio, A.; Dresselhaus, G.; Dresselhaus, M. S. Exciton–Photon, Exciton–Phonon Matrix Elements, and Resonant Raman Intensity of Single-Wall Carbon Nanotubes. *Phys. Rev. B* **2007**, *75*, 035405.
50. Saito, R.; Dresselhaus, G.; Dresselhaus, M. S. Trigonal Warping Effect of Carbon Nanotubes. *Phys. Rev. B* **2000**, *61*, 2981–2990.
51. Reich, S.; Thomsen, C. Chirality Dependence of the Density-of-States Singularities in Carbon Nanotubes. *Phys. Rev. B* **2000**, *62*, 4273–4276.
52. Zucker, J. E.; Pinczuk, A.; Chemla, D. S. Relation of Resonant Raman Line-Shape to Electronic Structure in Quantum Wells. *Phys. Rev. B* **1988**, *38*, 4287–4290.
53. Haroz, E. H.; Bachilo, S.; Weisman, R. B.; Doorn, S. K. Curvature Effects on the E_{33} and E_{44} Exciton Transitions in Semiconducting Single-Walled Carbon Nanotubes. *Phys. Rev. B* **2008**, *77*, 125405.
54. Telg, H.; Maultzsch, J.; Reich, S.; Thomsen, C. Resonant Raman Intensities and Transition Energies of the E11 Transitions in Carbon Nanotubes. *Phys. Rev. B* **2006**, *74*, 115415.